ADVANCED FUNCTIONAL MATERIALS
www.afm-journal.de

Inducing and Probing Localized Excitons in Atomically Thin Semiconductors via Tip-Enhanced Cavity-Spectroscopy

Hyeongwoo Lee, Inki Kim, Chulho Park, Mingu Kang, Jinseong Choi, Kwang-Yong Jeong, Jungho Mun, Yeseul Kim, Jeonghoon Park, Markus B. Raschke, Hong-Gyu Park, Mun Seok Jeong, Junsuk Rho, and Kyoung-Duck Park**

In atomically thin semiconductors, localized exciton (X_L) coupled to light provides a new class of optical sources for potential applications in quantum communication. However, in most studies, X_L photoluminescence (PL) from crystal defects has mainly been observed in cryogenic conditions because of their sub-wavelength emission region and low quantum yield at room temperature. Hybrid-modality of cavity-spectroscopy to induce and probe the X_L emissions at the nanoscale in atomically thin semiconductors is presented. By placing a WSe_2 monolayer on the two extremely sharp Au tips in a bowtie antenna with a radius of curvature of <1 nm, tensile strain of ≈0.3% is effectively induced in a <30 nm region to create robust X_L states. The Au tip then approaches the strained crystal region to enhance the X_L emissions and probe them with tip-enhanced photoluminescence (TEPL) spectroscopy at room temperature. Through this triple-sharp-tips cavity-spectroscopy with <15 nm spatial resolution, TEPL enhancement as high as ≈4.0×10^4 by the Purcell effect is achieved, and peak energy shifts of X_L up to ≈40 meV are observed. This approach combining nano-cavity and -spectroscopy provides a systematic way to induce and probe the radiative emission of localized excitons in 2D semiconductors offering new strategies for dynamic quantum nano-optical devices.

1. Introduction

Ever since photoluminescence (PL) responses of localized exciton (X_L) were observed in naturally occurring crystal defects and edges in atomically thin semiconductors,[1–4] their unique single photon emitting behaviors in a fascinating 2D platform have attracted a lot of attentions for their potential applications in quantum information and communication devices.[5] In addition, recent studies have demonstrated that the X_L can be deterministically induced at any desired locations. For instance, the X_L emission was observed by transferring atomically thin semiconductors on the nano-structures through the induced artificial strain.[6–9] Furthermore, a nanocube cavity array was exploited to induce strain and drive more efficient X_L emission through Purcell enhancement.[10]

However, these studies have only been performed at cryogenic temperatures because of the small exciton binding energy of X_L,[11] which leads to a much lower quantum yield at room temperature compared to the overwhelming radiative emission of neutral exciton (X_0).[12,13] Since these low-temperature operations heavily restrict the practical application of single photon emitting devices, there have been significant efforts to observe the X_L emission at room temperature. To probe the weak X_L emission at room temperature, local near-field PL measurements are the only possible approach up to the present. For instance, the defect bound excitons in a WS_2 monolayer

H. Lee, M. Kang, J. Choi, Prof. K.-D. Park
Department of Physics
Ulsan National Institute of Science and Technology (UNIST)
Ulsan 44919, Republic of Korea
E-mail: kdpark@unist.ac.kr

Dr. I. Kim, Y. Kim, J. Park, Prof. J. Rho
Department of Mechanical Engineering
Pohang University of Science and Technology (POSTECH)
Pohang 37673, Republic of Korea
E-mail: jsrho@postech.ac.kr

C. Park
Department of Energy Science
Sungkyunkwan University (SKKU)
Suwon 16419, Republic of Korea

K.-Y. Jeong, Prof. H.-G. Park
Department of Physics
Korea University
Seoul 02841, Republic of Korea

J. Mun, Prof. J. Rho
Department of Chemical Engineering
Pohang University of Science and Technology (POSTECH)
Pohang 37673, Republic of Korea

Prof. M. B. Raschke
Department of Physics, Department of Chemistry, and JILA
University of Colorado
Boulder, CO 80309, USA

Prof. M. S. Jeong
Department of Physics and Energy Engineering
Hanyang University
Seoul 04763, Republic of Korea

The ORCID identification number(s) for the author(s) of this article can be found under https://doi.org/10.1002/adfm.202102893.

DOI: 10.1002/adfm.202102893

(ML) were spatially resolved using a near-field scanning optical microscopy (NSOM) with ≈70 nm spatial resolution.[14] In this work, it was found that the X_L emission properties are strongly modulated by the structural features of the crystal defects. In addition, the strain-induced X_L emissions at nanobubbles were probed using tip-enhanced photoluminescence (TEPL) approach.[15] Through higher spatial resolution (≈34 nm) nano-imaging and -spectroscopy, they revealed the correlation between the X_L emission properties and the strain-induced confinement potential distribution with the support of a theoretical model, yet with the limitation of the low optical sensitivity and capability of artificially inducing the X_L emission. Therefore, it is highly desirable to deterministically induce and probe the X_L emission with high optical sensitivity and nanoscale spatial resolution at room temperature.

Here, we present hybrid-modality of cavity-spectroscopy to induce and probe the room temperature X_L emissions at the nanoscale in atomically thin semiconductors. To date, as can be seen in previous studies,[10,14,15] the static cavity and far-field or near-field spectroscopy were independently studied with their own weaknesses. Through this novel concept of cavity-spectroscopy, we overcome the weaknesses of both the static cavity and optical spectroscopy.[16] Specifically, the localized states of excitons in a WSe_2 ML are deterministically created by inducing a confinement potential on the nanoscale region using extremely sharp bowtie tips.[17,18] We then form the triple-sharp-tips plasmonic cavity by adding a position-controllable Au tip on the bowtie nano-gap with <15 nm resolution TEPL spectroscopy modality.[19,20] In this case, the radiative emission rate of the X_L is highly enhanced by the Purcell effect of the ultracompact cavity.[21–25] TEPL spectroscopy then probes the X_L emission at room temperature with ≈4.0×10^4-fold PL enhancement.

2. Results

2.1. Triple-Sharp-Tips Geometry for Deterministic X_L Emissions

To induce artificial nanoscale strain in WSe_2 ML, we use sharp tips in an Au bowtie structure fabricated by cascade domino lithography, which overcomes long-standing challenge of sub-nanometer tip fabrication.[17] The tips in the bowtie structure have a gap size of ≈5–20 nm with a radius of curvature (RoC) of <1 nm (see Supporting Information for optical properties). When the WSe_2 ML is transferred to this extremely sharp structure, the locally induced strain forms a potential well, which can bound excitons tightly on the nanoscale.[6,9,18] To couple optical fields effectively to these X_L and detect their PL responses, we use TEPL spectroscopy, as illustrated in **Figure 1**a.[26] The electrochemically etched Au tip is positioned on the nano-gap to form the triple-sharp-tips geometry and able to control the distance between tip and sample with <0.2 nm precision using shear-force atomic force microscopy (AFM) feedback (see Experimental Section for details).

When a linearly polarized excitation beam (632.8 nm), polarized parallel with respect to the tip axis, is focused onto the triple-sharp-tips structure, both in-plane and out-of-plane optical fields are strongly localized which enable us to measure TEPL response of X_0 and X_L. We confirm the capping condition of the transferred crystal on the nano-gap through AFM and scanning electron microscopy (SEM) measurements, as shown in Figure 1b–f. As can be seen in the high-resolution 2D images and topographic line profiles, the ML crystal uniformly covers the bowtie structure and forms a steep curve at the nano-gap. Figure 1g shows an illustration of the steeply curved WSe_2 ML formed at the nano-gap of the bowtie antenna. Due to

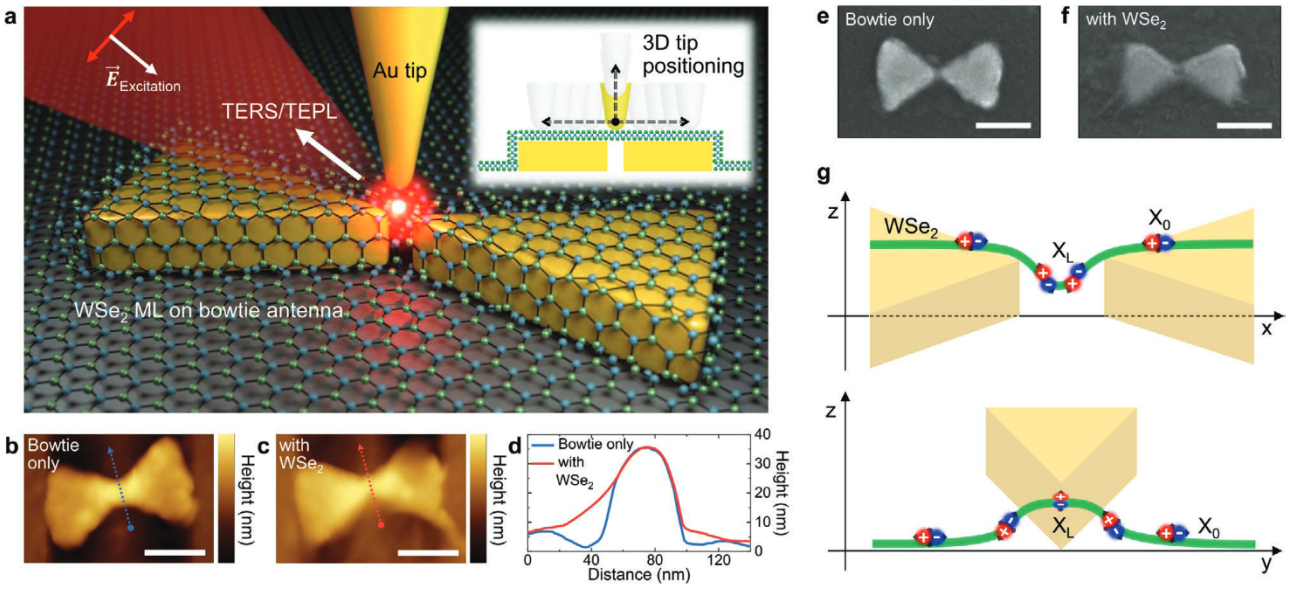

Figure 1. Experimental schematic of the triple-sharp-tips structure with a WSe_2 ML. a) Schematic of tip-enhanced nano-spectroscopy and triple-sharp-tips structure to induce and probe the radiative emissions of localized excitons in a WSe_2 ML. The Au tip position can be controlled three-dimensionally through shear-force AFM feedback. AFM images of the bowtie nano-antenna without (b) and with (c) a WSe_2 ML and corresponding AFM line profiles (d) across the bowtie nano-gap derived from (b) and (c). SEM images of the bowtie nano-antenna without (e) and with (f) a WSe_2 ML. The transferred crystal clings tight on the sharp nano-gap. Scale bars are 100 nm. g) Detailed schematic of the sharply curved WSe_2 crystal at the nano-gap and the distribution of X_0 and X_L at the localized confinement potential.

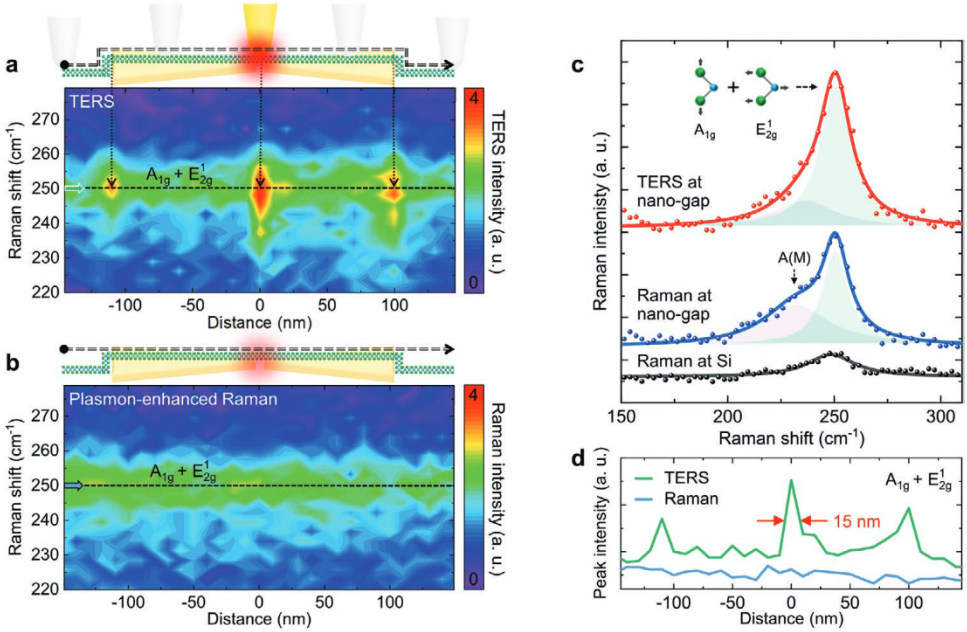

Figure 2. Probing the effect of sloping down regions of a WSe_2 ML with TERS measurement. Spectral TERS (a) and plasmon-enhanced Raman (b) line traces along the longitudinal center axis of the bowtie antenna with a WSe_2 ML measured at room temperature. c) TERS (red) and plasmon-enhanced Raman (blue) spectra of a WSe_2 ML at the nano-gap with the Voigt fitting, exhibiting a significant enhancement of degenerated A_{1g} and E^1_{2g} mode in the TERS spectrum. Far-field Raman spectrum of a WSe_2 ML on the Si substrate is shown for comparison. d) TERS (green) and plasmon-enhanced Raman (blue) intensity profiles of the degenerated $A_{1g} + E^1_{2g}$ peak, derived from the dashed lines in (a) and (b), exhibiting the sloping regions of the crystal on the bowtie antenna with TERS spatial resolution of <15 nm.

the locally induced strain and the created confinement potential, neutral excitons are drifted and bound to that nanoscale region as a form of the localized exctons.[15] The polarization of the X_L trapped in the confinement potential is affected by the spatial distribution of the potential well.[9,18] In our complicated anisotropic crystal geometry, the X_L dipoles at the center region of nano-gap are expected to be linearly polarized along the longitudinal bowtie axis[9] and the X_L dipoles at the steeply curved regions are polarized along the slopes, as illustrated in Figure 1g.

2.2. Nano-Chemical Characterization of the Structure of Transferred WSe_2 Monolayer

Figure 2a shows a spectral variation of tip-enhanced Raman spectroscopy (TERS) responses for a WSe_2 ML when the Au tip moves along the longitudinal axis of the bowtie antenna. The distinct TERS response of the $A_{1g} + E^1_{2g}$ mode (≈250 cm^{-1}, degenerate mode for out-of-plane vibration of Se atoms and in-plane vibration of W and Se atoms[27,28]) is observed in the nano-gap and both edges of the bowtie antenna. These three spots correspond to the slipping down regions of the transferred crystal.

In contrast, this spatial heterogeneity cannot be resolved in the plasmon-enhanced Raman profile (Figure 2b) due to the resolution limit. To understand the physical mechanism of the strong TERS response in the three local regions, we investigate spectral features by plotting TERS (red) and plasmon-enhanced Raman (blue) spectra in the nano-gap as shown in Figure 2c. While the A(M) mode (≈235 cm^{-1}, asymmetric phonon mode at the M point[29,30]) shows no distinct enhancement, the $A_{1g} + E^1_{2g}$ mode shows significant signal enhancement in the TERS measurement. In the nano-gap, the vibration direction of the out-of-plane Raman mode (A_{1g}) and in-plane Raman mode (E^1_{2g}) are not matched with the polarization axis of the nano-gap plasmon in the bowtie antenna because of the rotated geometry of the 2D crystal caused by the dramatic sloping down structure. The strong enhancement of TERS intensity in the nano-gap well indicates the effect of the tip which enhances the *z*-polarized near-field dominantly. Therefore, we can assume that the E^1_{2g} mode is the dominant vibrational mode in the TERS peak of the $A_{1g} + E^1_{2g}$ mode. That is, the E^1_{2g} mode is in parallel with respect to the tip-axis and the dominant near-field polarization.[31] Figure 2d shows TERS (green) and plasmon-enhanced Raman (blue) intensity profiles for the $A_{1g} + E^1_{2g}$ peak to quantify the spatial resolution of our approach, that is, < 15 nm.

2.3. Radiative Emissions of X_L at Room Temperature

Figure 3a shows a variation of the TEPL spectra of the WSe_2 ML when the Au tip moves along the longitudinal axis of the bowtie antenna. When the tip is located on the Au surface of the bowtie antenna, the TEPL signal of X_0 is observed, yet with no PL response of X_L. In contrast, the pronounced spectral change in TEPL signal is observed when the tip is located above the nano-gap. As indicated in Figure 3a (dashed box, X_L), the additional lower-energy shoulder emerges near the nano-gap which corresponds to the radiative emission of X_L.

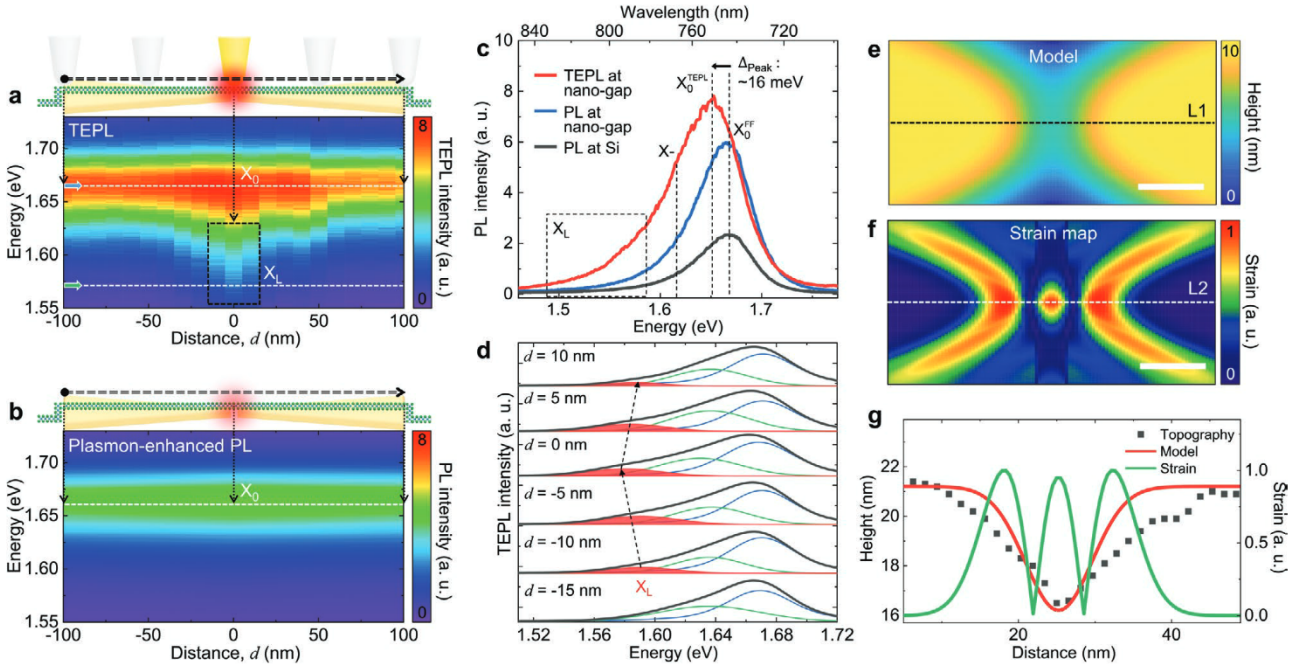

Figure 3. Probing radiative emission of localized excitons with TEPL measurement. Spectral TEPL (a) and plasmon-enhanced PL (b) line traces along the longitudinal center axis of the bowtie antenna with a WSe_2 ML measured at room temperature. c) TEPL and plasmon-enhanced PL spectra of a WSe_2 ML at the nano-gap, derived from (a) and (b), exhibiting a red-shift of the neutral exciton peak (X_0) and the new emerging localized exciton peak (X_L) in the TEPL spectrum. Far-field PL spectrum of a WSe_2 ML on the Si substrate is shown for comparison. d) Fitted TEPL spectra of X_0 (blue), X- (green) and X_L (red) peaks, derived from (a), exhibiting the nanoscale spatial extent of the radiative emission of the localized excitons and existence of the potential minima. Modeled morphology (e) and calculated strain map (f) of the WSe_2 ML on the bowtie structure based on the measured AFM topography (Figure S1a, Supporting Information). Scale bar is 10 nm. g) Line profiles of the measured AFM topography (black dot), modeled morphology derived from L1 in (e) (red), and strain derived from L2 in (f) (green).

On the other hand, the X_L emission is not observed in the plasmon-enhanced far-field PL spectra (Figure 3b) due to the diffraction limited spatial resolution. To investigate the modified spectral feature with the triple-sharp-tips structure in detail, we compare the plasmon-enhanced far-field PL and TEPL spectra in the nano-gap (derived from Figure 3a,b), as shown in Figure 3c. As for the comparison with a far-field PL spectrum of a WSe_2 ML on Si substrate (black), a significant PL enhancement of the X_0 is observed with the bowtie antenna (blue) owing to the strong in-plane field localization in the nano-gap, yet with no modification of spectral shape. In contrast, the TEPL spectrum (red) shows a peak shift of neutral exciton (X_0: from ≈1.667 to ≈1.651 eV), as well as new emerging shoulders of the localized excitons (X_L at ≈1.580 eV) and the trions (X- at ≈1.637 eV). Note that we assign the X- peak from the energy difference of ≈30 meV compared to the PL energy of the X_0, based on previous studies.[32–34] The observed spectral red-shift of ≈16 meV for the X_0 peak is attributed to the applied tensile strain in the nano-gap and corresponds to ≈0.3% strain based on previous studies.[35] This spectral shift cannot be observed in the plasmon-enhanced PL (Figure 3b) due to the limited spatial resolution in far-field measurement. We estimate the TEPL enhancement factor for the neutral excitons as high as $\approx 4.0 \times 10^4$, which is in good agreement with the theoretical estimation described in Figure 5 (see Supporting Information for more details).

To quantify the spatial extent of localized excitons in the strain induced region, we plot the evolution of fitted TEPL spectra for the X_0, X-, and X_L peaks, as shown in Figure 3d. The localized exciton emissions are observed at ≈20–30 nm region and show the lowest energy at the center of the nano-gap ($d = 0$ nm). The TEPL energy of X_L peak gradually increases as the probing location is far from the nano-gap center. The lowest energy of X_L at the center of the nano-gap and gradually increasing peak energy of X_L near the nano-gap region provide understanding for the spatial distribution of the confinement potential along the longitudinal axis of the bowtie.[9,18] To further investigate the spatial distribution of the confinement potential for the WSe_2 ML transferred on the bowtie structure, we calculate an anisotropic strain profile of the crystal.[18] First, we model a morphology of the WSe_2 ML on the bowtie structure (Figure 3e) based on the measured AFM topography (Figure S1a, Supporting Information). We then calculate the strain map from the morphology using continuum theory for a thin and elastic 2D sheet, as shown in Figure 3f (see Figures S1 and S2, Supporting Information, for more details). The obtained strain map shows the 3D potential confinement at the nano-gap center which can possibly facilitate single photon emissions.[18]. We then compare the line profiles of the measured topography, modeled morphology, and the calculated strain along the bowtie axis, as shown in Figure 3g. The strain profile for the corresponding morphology allows us to understand the local formation of the potential well at the nano-gap. This strain profile is in good agreement with the observed X_L emissions having the spatial extent of ≈20–30 nm (Figure 3d; see also Figure S3, Supporting Information, for TEPL intensity profile of X_L exhibiting ≈30 nm spatial extent).

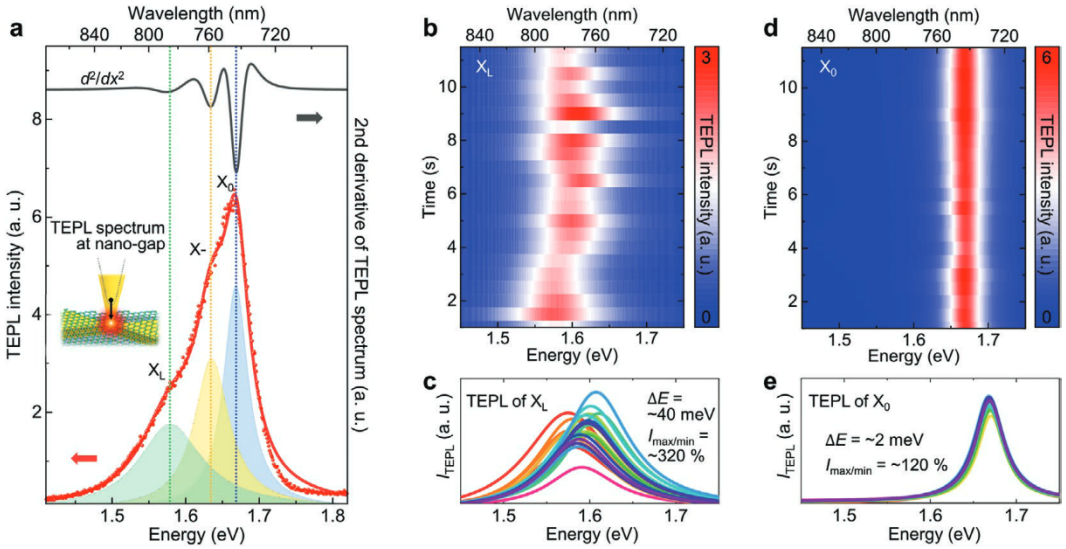

Figure 4. Inducing radiative emission of localized excitons with nano-optical antenna-tip control. a) TEPL spectrum of a WSe_2 ML in the triple-sharp-tips structure with a closely approached Au tip on the crystal (<1 nm) in the nano-gap. Neutral exciton (X_0, blue), trion (X-, yellow), and localized exciton (X_L, green) peaks are assigned through the fitting of the Voigt line shape function and reconfirmed with the second derivative of the TEPL spectrum (gray line). In the TEPL spectrum, red dots and red lines correspond to the measurement data and fit curve, respectively. b,d) TEPL evolution of the X_L and X_0 peaks with respect to time. To confirm the pronounced spectral fluctuation of the X_L peak in comparison with the X_0 peak, all the X_L and X_0 spectra (c,e) are derived with the Voigt fitting from the time-series data.

In the hyperspectral TEPL profiling (Figure 3a), the distance between the tip and sample is maintained at ≈3 nm with shear-force feedback. We then approach the Au tip further into the nano-gap to observe clearer TEPL spectrum from the triple-sharp-tips structure by increasing the field localization as well as the Purcell factor enhancement. **Figure 4**a shows the measured TEPL spectrum when the tip-sample distance is <1 nm. From fitting to the Voigt line shape function, we can derive distinct peaks of X_0 (blue), X- (yellow), and X_L (green) responses. In addition, we calculate the second derivative of the TEPL spectrum (black) to reconfirm the peak positions from them. As can be seen in Figure 4a, the minimum points of the second derivative curve exactly correspond to X_0, X-, and X_L peaks. The reproducibility of our deterministic X_L emission control is confirmed through the repeated experiments with different bowtie antennas (Figure S4, Supporting Information).

We then measure the TEPL spectra as a function of time at the fixed tip-sample distance to investigate spectral fluctuation and blinking behavior of the X_L PL. Figure 4b,d shows TEPL evolutions of the X_L and X_0 peaks derived from the Voigt fitting (see Figure S5, Supporting Information, for more details). While the X_0 peaks show stable emission in intensity and energy, the X_L peaks show distinct spectral and intensity fluctuations. All the emission spectra of X_L and X_0 over time are shown in Figure 4c,e to better visualize the spectral variation of the X_L peaks. Peak energy shifts are observed as large as ≈40 meV for the X_L peaks and ≈2 meV for the X_0 peaks. In addition, the ratio of maximum and minimum peak intensities are ≈320% and ≈120% for the X_L and X_0 peaks. Furthermore, the X_L emission shows a ≈2.5 × broader PL linewidth compared to the X_0 emission which is attributed to the existence of the local minima resulting in inhomogeneous distribution of exciton frequencies.[18,36] Therefore, the observed spectral fluctuations and broad linewidth of the X_L show the typical characteristics of localized excitons.[4,37]

2.4. Electromagnetic Simulations of the Optical Field and Radiative Decay Rate

To quantitatively investigate the optical properties of the triple-sharp-tips cavity, we model it (**Figure 5**a) and perform numerical analysis using finite-element method (FEM) for the field distribution and finite-difference time-domain (FDTD) for local density of states (LDOS) calculation (see Experimental Section for details). Note that we assume the gap size of the bowtie antenna for this simulation as 5 nm (see Figure S4, Supporting Information, for the gap size dependence of localized exciton emissions). When an excitation optical field (632.8 nm) is coupled to the cavity, electric charges of the Au nano-structures resonantly oscillate with the distribution, illustrated in Figure 5a. Figure 5b shows the simulated optical field intensity distribution of the cavity with a vector-field map to understand the excitation rate enhancement. In the cavity, the excitation field intensity is enhanced with the dominant out-of-plane optical field in the nano-gap between the etched tip and bowtie tips.

We simulate the decay-rate enhancement of a spontaneous emitter placed in the cavity (1.5 nm above the top surface of the bowtie antenna) with respect to the emission wavelength. Figure 5c,d shows the cross-sections of the total- (dashed) and radiative-decay-rate (solid) enhancement of the *x*- (blue) and *z*-axis (red) polarized dipole emitters for the bowtie only (c) and triple-sharp-tips (d) cavities. While the nonradiative-decay-rate ($\gamma^{nonrad} = \gamma^{tot} - \gamma^{rad}$) is quite large for both *x*- and *z*-polarized dipole emitters in the bowtie-only cavity (Figure 5c), the γ^{nonrad} in the triple-sharp-tips cavity is significantly decreased for the

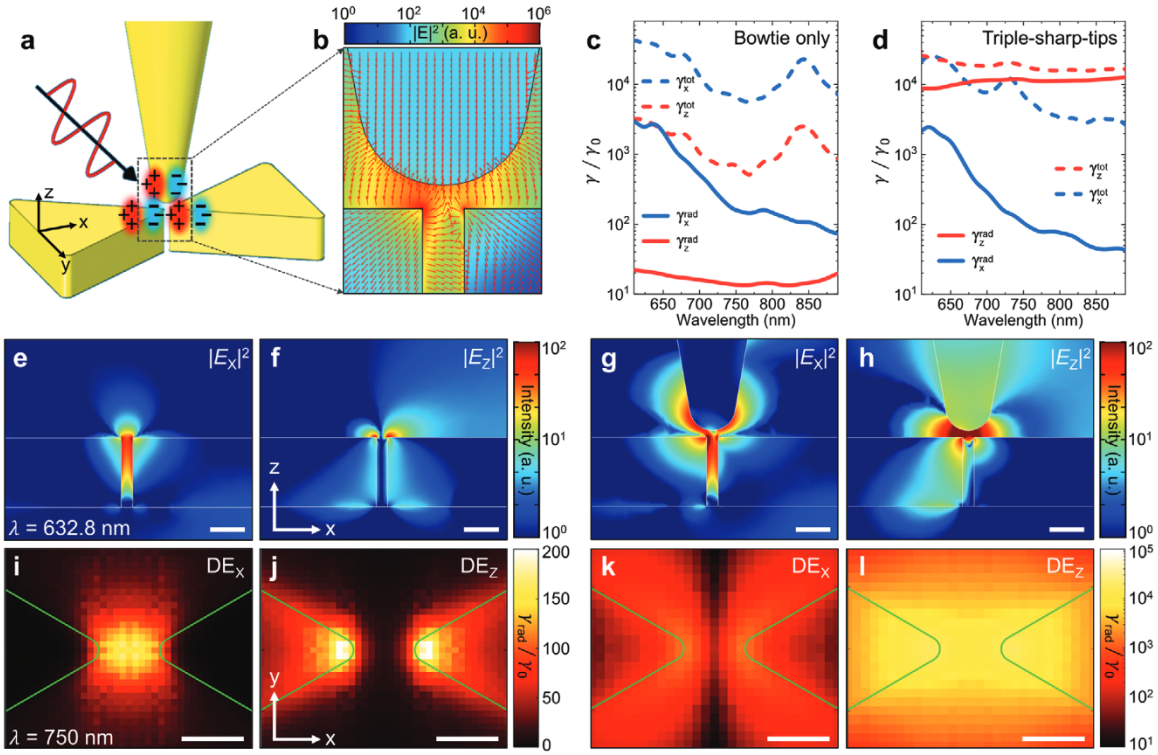

Figure 5. Electromagnetic simulations of the spatial optical properties in the triple-sharp-tips structure. a) The triple-sharp-tips model for three-dimensional numerical analysis of the field distribution of the excitation light and the radiative-decay-rate enhancement of the emission light. b) Simulated optical field intensity ($|E|^2$) distribution and vector-field map in the nano-gap of the triple-tips. c,d) Simulated cross-sections for the enhancement of total (dashed lines) and radiative (solid lines) decay rates in the nano-gap of the bowtie antenna (c) and triple-sharp-tips (d) structure. The cross-sections are simulated for the *x*- (blue) and *z*-polarized (red) dipole emitters placed 1.5 nm above the top surface of the bowtie antenna. Simulated in-plane (e,g) and out-of-plane (f,h) optical field intensity distributions in the bowtie antenna (e,f) and the triple-sharp-tips (g,h) structure. The wavelength of the excitation beam is fixed to 633 nm and scale bars are 15 nm. Simulated radiative-decay-rate enhancement (γ^{rad}/γ_0) distributions in the bowtie antenna (i,j) and triple-sharp-tips (k,l) structure for *x*- (i,k), and *z*-polarized (j,l) dipole emitters placed 1.5 nm above the top surface of the bowtie antenna. The wavelength of emission is fixed to 750 nm and scale bars are 5 nm. γ_0 is the initial decay rate.

z-polarized emitter γ_z^{tot} in Figure 5d because the reduced mode volume leads to increased Purcell factor of the cavity, which in turn gives rise to the enhanced γ^{rad}.[26]

We then calculate the in-plane and out-of-plane optical field intensity distribution separately to compare the excitation rate for X_0 ($|E_x|^2$) and X_L ($|E_z|^2$) in the cavities, as shown in Figure 5e–h. When the Au tip is added to the bowtie antenna, $|E_x|^2$ at 1.5 nm above the bowtie nano-gap (Figure 5g) shows comparable intensity with the bowtie-only antenna (Figure 5e). In contrast, $|E_z/E_0|^2$ is increased from ≈10 for the bowtie-only antenna to ≈10^2 for the triple-sharp-tips antenna by the added Au tip effect (Figure 5h) and we can estimate the excitation rate for X_L in our experiment.

Next, to quantify the enhanced spontaneous emission rate from the Purcell effect in our TEPL measurements, we simulate the distribution of the radiative-decay-rate enhancement (γ^{rad}/γ_0) for the *x*- and *z*-polarized dipole emitters (750 nm, 2D plane 1.5 nm above the top surface of the bowtie antenna) in both cavities, as shown in Figure 5i–l. Similar to the confirmed out-of-plane cavity effect on the excitation rate, we obtain γ^{rad}/γ_0 as high as ≈10^4 for the *z*-polarized emitter in the triple-sharp-tips cavity (Figure 5l). These simulated excitation and emission rates for the *z*-polarized emitters in the cavity explain the room temperature observation of X_L emission in our TEPL experiment.

In general, X_L PL is hard to observe at room temperature with far-field measurement because of the rapid decrease in quantum yield with increasing temperature, caused by thermal activation of carriers and low exciton binding energy of X_L.[12,13] On the other hand, the highly increased emission rate as well as the excitation field localization in the triple-sharp-tips cavity allows us to induce and probe X_L TEPL in our experiment.[10]

3. Discussions

Our experiment is designed to induce and probe the radiative emission of X_L at room temperature via cavity-spectroscopy. We fabricate extremely sharp bowtie tips[17] (RoC of <1 nm) and transfer a WSe_2 ML on it, to build a crystal structure having anisotropic strain at the nano-gap region. In this structure, the 3D confined potential induced by the anisotropic strain gives rise to the robust X_L emissions which are confirmed with confocal microscopy at ≈4K (see Figure S12, Supporting Information, for more details). Previous X_L studies demonstrated that the PL polarization is determined by the spatial distribution of the potential well due to the linearly oscillating behavior of the trapped excitons along the elongated potential well.[9,18] From the calculated strain map as well as recent

report,[9] we expect the X_L dipole emitters located at the symmetric center of the nano-gap are polarized along the longitudinal axis of the bowtie antenna. However, the other X_L emitters located in the steeply curved crystal structures, that is, near the nanoscale hill (in the transverse axis, Figure S2c, Supporting Information) and valley (in the longitudinal axis, Figure S2d, Supporting Information) geometries, are oriented mainly along the slopes. To explicitly characterize the dipole orientations, polarization-resolved PL measurement at the nanoscale is desirable, but the polarization-dependent TEPL measurement is not allowed because the wave vector conservation is lifted in plasmonic near-field measurements.[38]

In this nano-cavity device, we can significantly increase the excitation rate ($|E_z/E_0|^2 = \approx 10^2$) of the vertically oriented X_L owing to the strong out-of-plane field localization (Figure 5h). In addition, the quantum yield is largely enhanced by the Purcell effect because the effective mode volume in the triple-sharp-tips cavity is extremely small. We obtain ≈64% of enhanced quantum yield for the *z*-polarized dipole emitters located in triple-sharp-tips cavity ($Q_z = \gamma_z^{rad}/\gamma_z^{tot}$) from the electromagnetic simulation. For a chemical vapor deposition (CVD)-grown WSe_2 ML without the cavity, we adopt 0.2% of quantum yield ($Q_0 = \gamma_0^{rad}/\gamma_0^{tot}$) based on a previous study.[39] Hence, we can estimate a theoretical TEPL enhancement factor with the following formula by Zhang et al.:[40]

$$<\mathrm{EF}> = \left|\frac{E_z}{E_0}\right|^2 \times \frac{Q_Z}{Q_0}$$

The obtained ≈3.0×10^4-fold TEPL enhancement factor is in good agreement with the estimated TEPL enhancement factor from the measurement (≈4.0×10^4). Based on this mechanism, our triple-sharp-tips cavity in combination with TEPL nano-spectroscopy enables to induce and probe the X_L emissions. Moreover, precise 3D tip positioning (<0.2 nm) based on atomic force control provides the ability to dynamically engineer the cavity mode volume, field strength, and corresponding X_L emissions, as can be seen in the lateral (Figure 3a) and vertical (Figure 4a) tip-positioning effects.

4. Conclusion

In summary, we have demonstrated that ultracompact tip-enhanced nano-cavity spectroscopy with a triple-sharp-tips geometry gives access to localized states of excitons, beyond the limitations of previous X_L studies, such as observation at cryogenic temperature, limited spatial resolution, or the lack of systematic control. Most importantly, the carefully designed cavity structure with the ability to dynamically control the cavity mode volume (V) and corresponding radiative emission rate ($\propto 1/V$)[41–43] enables bright X_L emission and robust control of it at room temperature, which allow a range of device applications for quantum information technology. The presented cavity-spectroscopy approach (PL enhancement of ≈4.0×10^4) will be applied to greatly improve the efficiency and performance of quantum photonic devices.[44,45] In addition, the previously demonstrated electrically-driven single photon emission (i.e., electroluminescence) in 2D materials at cryogenic temperature[10,46–48] can be realized in ambient condition by adopting our cavity structure. Furthermore, our tip-enhanced nano-cavity and -spectroscopy approach can be extended to characterize other low-dimensional quantum materials, such as 0D quantum dots[49,50] and 1D quantum wires,[42] and induce and control their emitter-cavity interactions from the weak to the strong coupling regime.[20]

5. Experimental Section

Sample Preparation: To transfer the chemical vapor deposition (CVD)-grown WSe_2 monolayer onto a flat Au film/coverslip, a wet transfer process was used. As a first step, poly(methyl methacrylate) (PMMA) was spin-coated onto WSe_2 monolayer grown on the SiO_2 substrate. The PMMA-coated WSe_2 monolayer was then separated from the SiO_2 substrate using a hydrogen fluoride solution, and carefully transferred onto the bowtie device after being rinsed in distilled water to remove residual etchant. Then, it is dried naturally for 6 h to improve the adhesion. Lastly, the PMMA was removed using acetone.

Bowtie Fabrication: The sharp bowtie nanoantenna fabrication starts on a 500 µm thick silicon substrate. Using standard electron beam lithography (Elionix ELS-7800, acceleration voltage: 80 kV, beam current: 50 pA), the half bowtie patterns were defined on the copolymer (Microchem, MMA (8.5) MAA EL-8) / PMMA (Microchem, 495 PMMA A2) bilayer positive tone resist having different solubility in the developer. Such a bilayer process produces a T-shaped profile of the resist after development. The copolymer layer was spin-coated (5000 rpm, 60 s) and baked at 150 °C on the hotplate and its final thickness was about 250 nm. The PMMA layer was spin-coated (2000 rpm, 60 s) on the former copolymer layer and baked at 180 °C, its thickness was about 60 nm. After electron beam exposure, the copolymer/PMMA bilayer resist was developed in MIBK: IPA 1:3 solutions for 23 min at 4 °C. A cold development with a longer develop time enabled continuous development in the copolymer area affected by secondary electrons from the substrate while development in the PMMA layer was completed. As a result, a highly unstable T-shape resist profile could be made. The developed patterns were rinsed with IPA for 30 s, and to dry out the remaining liquid, nitrogen gas was blown on the patterned area directly. The unstable resist patterns collapsed, and the collapsed pillars leaned on the adjacent wall where half bowtie patterns were inscribed. This kind of process, called cascade domino lithography, can realize ultra-sharp-edged photoresist masks with single digit nanometer scale gap size. The junctions between the rounded edge planes of the pillar and wall formed a sharp gap spacing resist mask. On the mask, Cr (3 nm) and Au (50 nm) were deposited by electron beam evaporation (KVT KVE-ENS4004), followed by the standard lift-off process. The fabricated bowtie antenna had a 1 nm-radius of curvature and 5 nm gap size, which could not be realized by conventional electron beam lithography processes.

TERS/TEPL Setup: The prepared WSe_2 ML on bowtie antenna was loaded on a piezo-electric transducer (PZT, P-611.3x, Physik Instrumente) for XYZ scanning with <0.2 nm positioning precision. The Au tip (apex radius of ≈10 nm) fabricated with a refined electrochemical etching protocol was attached to a quartz tuning fork (resonance frequency of 32.768 kHz) to regulate the distance between the tip and sample under a shear-force AFM operated by a digital AFM controller (R9+, RHK Technology). For TEPL and TERS experiment, a conventional optical spectroscopy set-up was combined with the home-built shear-force AFM. For a high quality wavefront of the excitation beam, a He-Ne laser (632.8 nm, ≤1 mW) was coupled and passed through a single-mode fiber (core diameter of ≈3.5 µm) and collimated again using an aspheric lens. The collimated beam was then passed through a half-wave plate to make the excitation polarization parallel with respect to the tip axis. Finally, the beam was focused onto the Au tip using a microscope objective (NA=0.8, LMPLFLN100×, Olympus) with a side-illumination geometry. To ensure highly efficient laser coupling to the Au tip, the tip position was controlled with ≈30 nm precision by using Picomotor actuators (9062-XYZ-PPP-M, Newport). TEPL and TERS responses were collected using the same microscope objective (backscattering geometry) and

passed through an edge filter (LP02-633RE-25, Semrock) to cutoff the fundamental line. The signals were then dispersed onto a spectrometer (f = 328 mm, Kymera 328i, Andor) and imaged with a thermoelectrically cooled charge-coupled device (CCD, iDus 420, Andor) to obtain TEPL and TERS spectra. Before the experiment, the spectrometer was calibrated with a Mercury lamp. A 150 g/mm grating with 800 nm blazed (spectral resolution of 0.62 nm) and 600 g/mm grating with 500 nm blazed (spectral resolution of 3.75 cm^{-1}) were used for PL and Raman measurements, respectively.

Numerical Analysis: 3D full-wave simulations were performed to numerically analyze field enhancement and local density of states (LDOS) near the bowtie and the tip. Field enhancements (Figure 5b,e–h) were calculated using the Wave Optics module of COMSOL Multiphysics. A TM-polarized planewave incidence at 45° from air to a single bowtie with the tip was considered using the scattered field formulation surrounded by perfectly matched layer (or PML). LDOS (Figure 5c,d, i–l) were calculated using Lumerical FDTD. Total radiated power from an electric dipole and absorbed power to the total system were calculated to obtain the total and nonradiative decay rates.[51] Optical properties of silicon were taken from Palik,[52] and gold from Johnson and Christy.[53]

Supporting Information

Supporting Information is available from the Wiley Online Library or from the author.

Acknowledgements

H.L. and I.K. contributed equally to this work. This work was supported by the National Research Foundation of Korea (NRF) grants (2019K2A9A1A06099937 and 2020R1C1C1011301). J.R. acknowledges the NRF grants (2019R1A2C3003129, 2019M3A6B3030637, 2019R1A5A8080290) funded by the Ministry of Science and ICT (MSIT). I.K. acknowledges the NRF Sejong Science fellowship (NRF-2021R1C1C2004291) funded by the MSIT of the Korean government. Y.K. acknowledges a fellowship from Hyundai Motor Chung Mong-Koo Foundation and the POSTECHIAN fellowship from POSTECH. M.S.J. thanks the Creative Materials Discovery Program through NRF funded by the MSIT (2019M3D1A1078304). H.-G.P. acknowledges the NRF grants (2021R1A2C3006781 and 2020R1A4A2002828) funded by the MSIT. M.B.R. acknowledges support from the National Science Foundation (NSF Grant CHE-1709822). The authors thank D.S.L. and J.H.C. for the assistance of figure illustration.

Conflict of Interest

The authors declare no conflict of interest.

Data Availability Statement

Data available on request from the authors.

Keywords

cavity-spectroscopy, localized exciton, nano-cavity, plasmonic structures, purcell effect, tip-enhanced photoluminescence

Received: March 25, 2021
Revised: May 18, 2021
Published online: June 18, 2021

[1] Y.-M. He, G. Clark, J. R. Schaibley, Y. He, M.-C. Chen, Y.-J. Wei, X. Ding, Q. Zhang, W. Yao, X. Xu, C.-Y. Lu, J.-W. Pan, *Nat. Nanotechnol.* **2015**, *10*, 497.
[2] A. Srivastava, M. Sidler, A. V. Allain, D. S. Lembke, A. Kis, A. Imamoğlu, *Nat. Nanotechnol.* **2015**, *10*, 491.
[3] M. Koperski, K. Nogajewski, A. Arora, V. Cherkez, P. Mallet, J.-Y. Veuillen, J. Marcus, P. Kossacki, M. Potemski, *Nat. Nanotechnol.* **2015**, *10*, 503.
[4] P. Tonndorf, R. Schmidt, R. Schneider, J. Kern, M. Buscema, G. A. Steele, A. Castellanos-Gomez, H. S. van der Zant, S. M. de Vasconcellos, R. Bratschitsch, *Optica* **2015**, *2*, 347.
[5] L.-M. Duan, M. D. Lukin, J. I. Cirac, P. Zoller, *Nature* **2001**, *414*, 413.
[6] A. Branny, S. Kumar, R. Proux, B. D. Gerardot, *Nat. Commun.* **2017**, *8*, 15053.
[7] P. Tonndorf, O. Del Pozo-Zamudio, N. Gruhler, J. Kern, R. Schmidt, A. I. Dmitriev, A. P. Bakhtinov, A. I. Tartakovskii, W. Pernice, S. Michaelis de Vasconcellos, R. Bratschitsch, *Nano Lett.* **2017**, *17*, 5446.
[8] Y. Luo, N. Liu, B. Kim, J. Hone, S. Strauf, *Nano Lett.* **2020**, *20*, 5119.
[9] J.-P. So, K.-Y. Jeong, J. M. Lee, K.-H. Kim, S.-J. Lee, W. Huh, H.-R. Kim, J.-H. Choi, J. M. Kim, Y. S. Kim, C.-H. Lee, S.-W. Nam, H.-G. Park, *Nano Lett.* **2021**, *21*, 1546.
[10] Y. Luo, G. D. Shepard, J. V. Ardelean, D. A. Rhodes, B. Kim, K. Barmak, J. C. Hone, S. Strauf, *Nat. Nanotechnol.* **2018**, *13*, 1137.
[11] J. Huang, T. B. Hoang, M. H. Mikkelsen, *Sci. Rep.* **2016**, *6*, 22414.
[12] J. Pandey, A. Soni, *Appl. Surf. Sci.* **2019**, *463*, 52.
[13] J. S. Ross, S. Wu, H. Yu, N. J. Ghimire, A. M. Jones, G. Aivazian, J. Yan, D. G. Mandrus, D. Xiao, W. Yao, X. Xu, *Nat. Commun.* **2013**, *4*, 1474.
[14] Y. Lee, S. J. Yun, Y. Kim, M. S. Kim, G. H. Han, A. Sood, J. Kim, *Nanoscale* **2017**, *9*, 2272.
[15] T. P. Darlington, C. Carmesin, M. Florian, E. Yanev, O. Ajayi, J. Ardelean, D. A. Rhodes, A. Ghiotto, A. Krayev, K. Watanabe, *Nat. Nanotechnol.* **2020**, *15*, 854.
[16] M. Rahaman, R. D. Rodriguez, G. Plechinger, S. Moras, C. Schuller, T. Korn, D. R. Zahn, *Nano Lett.* **2017**, *17*, 6027.
[17] I. Kim, J. Mun, K. M. Baek, M. Kim, C. Hao, C.-W. Qiu, Y. S. Jung, J. Rho, *Mater. Today* **2020**, *39*, 89.
[18] J. Kern, I. Niehues, P. Tonndorf, R. Schmidt, D. Wigger, R. Schneider, T. Stiehm, S. Michaelis de Vasconcellos, D. E. Reiter, T. Kuhn, *Adv. Mater.* **2016**, *28*, 7101.
[19] H. Lee, D. Y. Lee, M. G. Kang, Y. Koo, T. Kim, K.-D. Park, *Nanophotonics* **2020**, *9*, 3089.
[20] K.-D. Park, M. A. May, H. Leng, J. Wang, J. A. Kropp, T. Gougousi, M. Pelton, M. B. Raschke, *Sci. Adv.* **2019**, *5*, eaav5931.
[21] E. M. Purcell, H. C. Torrey, R. V. Pound, *Phys. Rev.* **1946**, *69*, 37.
[22] G. M. Akselrod, C. Argyropoulos, T. B. Hoang, C. Ciracì, C. Fang, J. Huang, D. R. Smith, M. H. Mikkelsen, *Nat. Photon.* **2014**, *8*, 835.
[23] J. Sun, H. Hu, D. Zheng, D. Zhang, Q. Deng, S. Zhang, H. Xu, *ACS Nano* **2018**, *12*, 10393.
[24] G. M. Akselrod, T. Ming, C. Argyropoulos, T. B. Hoang, Y. Lin, X. Ling, D. R. Smith, J. Kong, M. H. Mikkelsen, *Nano Lett.* **2015**, *15*, 3578.
[25] J. Huang, G. M. Akselrod, T. Ming, J. Kong, M. H. Mikkelsen, *ACS Photon.* **2018**, *5*, 552.
[26] K.-D. Park, T. Jiang, G. Clark, X. Xu, M. B. Raschke, *Nat. Nanotechnol.* **2018**, *13*, 59.
[27] H. Sahin, S. Tongay, S. Horzum, W. Fan, J. Zhou, J. Li, J. Wu, F. Peeters, *Phys. Rev. B* **2013**, *87*, 165409.
[28] E. Del Corro, H. Terrones, A. Elias, C. Fantini, S. Feng, M. A. Nguyen, T. E. Mallouk, M. Terrones, M. A. Pimenta, *ACS Nano* **2014**, *8*, 9629.
[29] H. Terrones, E. Del Corro, S. Feng, J. Poumirol, D. Rhodes, D. Smirnov, N. Pradhan, Z. Lin, M. Nguyen, A. Elias, T. E. Mallouk, L. Balicas, M. A. Pimenta, M. Terrones, *Sci. Rep.* **2014**, *4*, 4215.

[30] X. Zhang, X.-F. Qiao, W. Shi, J.-B. Wu, D.-S. Jiang, P.-H. Tan, *Chem. Soc. Rev.* **2015**, *44*, 2757.
[31] L. Tong, X. Duan, L. Song, T. Liu, L. Ye, X. Huang, P. Wang, Y. Sun, X. He, L. Zhang, K. Xu, W. Hu, J.-B. Xu, J. Zang, G. J. Cheng, *Appl. Mater. Today* **2019**, *15*, 203.
[32] W. Bao, N. J. Borys, C. Ko, J. Suh, W. Fan, A. Thron, Y. Zhang, A. Buyanin, J. Zhang, S. Cabrini, P. D. Ashby, A. Weber-Bargioni, S. Tongay, S. Aloni, D. F. Ogletree, J. Wu, M. B. Salmeron, P. J. Schuck, *Nat. Commun.* **2015**, *6*, 7993.
[33] A. M. Jones, H. Yu, N. J. Ghimire, S. Wu, G. Aivazian, J. S. Ross, B. Zhao, J. Yan, D. G. Mandrus, D. Xiao, W. Yao, X. Xu, *Nat. Nanotechnol.* **2013**, *8*, 634.
[34] Y. You, X.-X. Zhang, T. C. Berkelbach, M. S. Hybertsen, D. R. Reichman, T. F. Heinz, *Nat. Phys.* **2015**, *11*, 477.
[35] R. Schmidt, I. Niehues, R. Schneider, M. Drueppel, T. Deilmann, M. Rohlfing, S. M. De Vasconcellos, A. Castellanos-Gomez, R. Bratschitsch, *2D Mater.* **2016**, *3*, 021011.
[36] G. Moody, C. K. Dass, K. Hao, C.-H. Chen, L.-J. Li, A. Singh, K. Tran, G. Clark, X. Xu, G. Berghäuser, E. Malic, A. Knorr, X. Li, *Nat. Commun.* **2015**, *6*, 8315.
[37] Y. Luo, N. Liu, X. Li, J. C. Hone, S. Strauf, *2D Mater.* **2019**, *6*, 035017.
[38] K.-D. Park, M. B. Raschke, *Nano Lett.* **2018**, *18*, 2912.
[39] Y. Ye, Z. J. Wong, X. Lu, X. Ni, H. Zhu, X. Chen, Y. Wang, X. Zhang, *Nat. Photon.* **2015**, *9*, 733.
[40] Y. Zhang, W. Chen, T. Fu, J. Sun, D. Zhang, Y. Li, S. Zhang, H. Xu, *Nano Lett.* **2019**, *19*, 6284.
[41] J. A. Schuller, S. Karaveli, T. Schiros, K. He, S. Yang, I. Kymissis, J. Shan, R. Zia, *Nat. Nanotechnol.* **2013**, *8*, 271.
[42] Y. Luo, E. D. Ahmadi, K. Shayan, Y. Ma, K. S. Mistry, C. Zhang, J. Hone, J. L. Blackburn, S. Strauf, *Nat. Commun.* **2017**, *8*, 1413.
[43] M. Pelton, *Nat. Photon.* **2015**, *9*, 427.
[44] V. Zwiller, T. Aichele, O. Benson, *New J. Phys.* **2004**, *6*, 96.
[45] A. Schlehahn, A. Thoma, P. Munnelly, M. Kamp, S. Höfling, T. Heindel, C. Schneider, S. Reitzenstein, *APL Photon.* **2016**, *1*, 011301.
[46] J. S. Ross, P. Klement, A. M. Jones, N. J. Ghimire, J. Yan, D. Mandrus, T. Taniguchi, K. Watanabe, K. Kitamura, W. Yao, X. Xu, *Nat. Nanotechnol.* **2014**, *9*, 268.
[47] B. W. Baugher, H. O. Churchill, Y. Yang, P. Jarillo-Herrero, *Nat. Nanotechnol.* **2014**, *9*, 262.
[48] A. Pospischil, M. M. Furchi, T. Mueller, *Nat. Nanotechnol.* **2014**, *9*, 257.
[49] K. J. Vahala, *Nature* **2003**, *424*, 839.
[50] Ł. Dusanowski, D. Köck, E. Shin, S.-H. Kwon, C. Schneider, S. Höfling, *Nano Lett.* **2020**, *20*, 6357.
[51] D. L. Mack, E. Cortés, V. Giannini, P. Török, T. Roschuk, S. A. Maier, *Nat. Commun.* **2017**, *8*, 14513.
[52] D. P. Edward, I. Palik, *Handbook of optical constants of solids*, Elsevier Science, Amsterdam **1985**.
[53] P. B. Johnson, R.-W. Christy, *Phys. Rev. B* **1972**, *6*, 4370.